

Evidence of High Shear Velocity Anomalies Inside the Pacific LLSVP

Rafael Abreu ^{*,1}, Mariano S. Arnaiz-Rodríguez¹ and Chahana Nagesh¹

¹*Institut de Physique du Globe de Paris, CNRS, Université de Paris, Paris, France*

Abstract

We present the evidence of high-velocity regions within the Pacific Large Low Seismic Velocity Province (LLSVP), uncovered using the Virtual Receiver Approach (VRA), a novel seismic imaging method that allows us to determine local absolute velocity values of a non-reflecting body wave that are independent of any assumed Earth model. Our results reveal a complex dynamics of high- and low-velocity regions within the Pacific LLSVP. While low-shear-wave velocities dominate, consistent with the traditionally understood nature of LLSVPs, we identify distinct high-velocity anomalies—an observation not previously reported in this region. We interpret these anomalies as lateral compositional variations within the LLSVP. Petrological modeling suggests that high-velocity regions are associated with low FeO content, potentially linked to the inclusion of post-perovskite material driven by mantle convection. Alternatively, remnants of subducted oceanic crust (e.g., MORB) could also explain the observed features. Conversely, low-velocity anomalies correspond to FeO-rich compositions. Our findings highlight the thermochemical heterogeneity of the LLSVP, revealing a more complex internal structure than previously thought. The application of the VRA is able to resolve fine-scale structures that have remained a biggest challenge in global tomographic models.

Key words: seismic arrays, seismic imaging, composition of the Earth

^{*}email: rabreu@ipgp.fr

1 Introduction

Mantle convection is a fundamental process in Earth's geodynamics. It is strong enough to drive the vigorous plate tectonics shaping the planet's surface while being slow enough to retain heat trapped in the core (Parsons and McKenzie, 1978; Turcotte and Schubert, 2002; Lay et al., 2008). Understanding its dynamics is a monumental challenge, as the mantle is more inaccessible than the farthest observable stars or the deepest parts of the ocean. Decades of research have provided a broad understanding of Earth's lower mantle (Dziewonski et al., 1977; Frost et al., 2004; Kesson et al., 1998; Helffrich and Wood, 2001; Garnero and McNamara, 2008; Tsuchiya et al., 2004; Hirose et al., 1999). This region, spanning from the transition zone (410 km to 670 km) to the core-mantle boundary (CMB) at 2891 km depth, exhibits relatively smooth seismic velocity and density gradients compare to the highly heterogeneous crust (Davies and Dziewonski, 1975; Dziewonski et al., 1977; Garnero and McNamara, 2008), largely due to the stability of magnesium-silicate perovskite under extreme temperature and pressure (Kaminsky, 2012; Kesson et al., 1998; Murakami et al., 2012). Near the CMB, seismic velocities become more complex, with abrupt increases attributed to a phase transition to the post-perovskite phase and pronounced thermal and chemical heterogeneity in the boundary layer above the CMB, known as the D'' region (Oganov and Ono, 2004; Itaya et al., 2004; Murakami et al., 2004). However, much remains to be learned about this deep region of Earth.

Large low-seismic-velocity provinces (LLSVPs) are distinctive structures of the lowermost mantle (Garnero and Helmberger, 1995; Ritsema et al., 1999; Garnero and McNamara, 2008; Lay et al., 2006; Sun and Miller, 2013; He and Wen, 2009; McNamara et al., 2010; Avants et al., 2006), that span thousands of kilometers laterally and possibly extend up to 1000 km vertically from the CMB (Thorne et al., 2013b). They are characterized by reduction in S-wave and P-wave velocities and sharp edges (Ni et al., 2002; Wang and Wen, 2004; King and Anderson, 1998; Frost and Rost, 2014; Sun and Miller, 2013), corresponding to the base of deep mantle plumes (Burke et al., 2008; He and Wen, 2009; Ford et al., 2006; He et al., 2006)

Furthermore, LLSVPs may contain ultra-low-velocity zones (ULVZs), characterized by extreme reductions in seismic velocities (up to -30% for S-waves and -10% for P-waves) and likely increases in density (Brown et al., 2015; Jensen et al., 2013; Rost et al., 2010, 2006; Rost and Garnero, 2006; Rost and Revenaugh, 2003). These ULVZs lie near the CMB with variable shapes, widths, and distributions (Wen and Helmberger, 1998; McNamara et al., 2010; Zhang et al., 2009; Vanacore et al., 2016; Mao et al., 2006; Garnero et al., 1998). They are challenging to detect and characterize through global tomographic studies (Ritsema et al., 1999, 2011; Bozdağ et al., 2016; French and Romanowicz, 2014).

Currently, the structure, origin, and convective nature of the LLSVPs and ULVZs are still a matter of debate. Different possible origins have been proposed: (i) compositional in nature (Ritsema et al., 1999; Ishii and Tromp, 2004); (ii) thermochemical (Davaille et al., 2003; Hansen and Yuen, 2000); and (iii) lithospheric subducted material (Maruyama et al., 2007b; Tanaka et al., 2009). LLSVPs seem to be compositionally subdivided into two domains: a primordial bottom domain near the core-mantle boundary (serving as an isolated reservoir with distinctive isotopic compositions (Burke et al., 2008), and a basaltic shallow (perhaps thermally buoyant; McNamara and Zhong (2004, 2005)) domain that extends from 1100 to 2300 km depth (Ballmer et al., 2016a). Whereas ULVZs may be part of internal convection mechanisms within the larger velocity anomalies (McNamara et al., 2010; Thorne et al., 2013a). In any case, it is clear that, to properly understand the convection system of the lower mantle, it is important to comprehend the origin, composition, physical properties, and role that LLSVPs and ULVZs play. To achieve this, it is of primary importance to illuminate and image the structures in Earth's lower mantle.

One of the most powerful tools for imaging Earth's interior is seismic tomography. Emerging in the 1970s, this method revolutionized our understanding of the 3D distribution of physical properties affecting seismic wave propagation, such as elasticity, anelasticity, anisotropy, and density. Seminal studies by Aki et al. (1977) and Dziewonski et al. (1977); Dziewonski (1984) laid the foundation for this field. While Aki and colleagues focused on regional-scale structures, Dziewonski and his team produced the first images of the lower mantle, revealing early on the existence of the two LLSVPs (originally referred to as "superplumes"). Since then, tomographic models often play a critical role in the analysis of the subsurface, aiding in the estimation of lithology, temperature, and fluid content while providing a snapshot of present-day mantle dynamics. Tomography usually presents results in terms of velocity anomalies that are conditioned on the initial model used, parametrization of the studied space, inverse method used, and seismological theory employed (ray theory, finite frequency, or full waveform).

The interpretation of velocity anomalies can be misleading. For example, high-shear-velocity regions, like shields, can appear as cold and sinking but are actually chemically buoyant. Stronger S-wave velocity reductions in the deep mantle may suggest chemical differences, melt, or high temperatures. This is why it becomes important to try to estimate the lower mantle's absolute velocity values.

In this study, we present a new method, the Virtual Receiver Approach (VRA), that allows us to sample the velocity field at depth from teleseismic travel-time data recorded at neighboring stations. We will show that our VRA is replicable, efficient, accurate, robust, and easy to implement. We begin by laying the fundamentals of our approach and validating it. We proceed to test it to probe the lower mantle beneath the Pacific Ocean, aiming to estimate the absolute shear wave velocity of the Pacific LLSVPs. Finally, we attempt to interpret these results in terms of compositional anomalies and temperature conditions.

2 Methodology: The Virtual Receiver Approach

We introduce an imaging methodology that we call The Virtual Receiver Approach based on the concept of the slowness vector u defined as follows (Rost and Thomas, 2002)

$$u = \frac{1}{v_{\text{app}}} = \frac{\sin(i)}{v_0}, \quad (1)$$

where v_{app} is the apparent velocity, i is the angle of incidence of the ray and v_0 the velocity of the medium (see Fig. 1-a).

The slowness u (eq. (1)) is constant along the ray path and it is equal to the inverse of the medium velocity v_0 when $\sin(i) = 1$, i.e., when the wave does not reflect at an interface and travels horizontally ($i_d = 90^\circ$), at the deepest point of the ray (see Fig. 1-a). Therefore, the velocity of the medium at the deepest point of the ray v_d is equal to the inverse of the slowness $v_d = 1/u$ (Stein and Wysession, 2009; Rost and Thomas, 2002).

If we consider a 1D isotropic layered medium, the slowness u in eq. (1) can be approximated as follows (Mula and Müller, 1980; Souriau and Poupinet, 1994)

$$u(x_0) \approx \frac{t_1 - t_2}{d_1 - d_2} = \frac{\Delta t}{\Delta d}, \quad (2)$$

where t_1, t_2 are the arrival times of the wave of interest at two stations 1 and 2 located at positions x_1, x_2 , respectively and with epicentral distances d_1, d_2 .

Equation (2) can be understood in three (fundamental) different ways depending on the interpretation of the location x_0 : If one assumes that $x_0 = x_1$ and/or $x_0 = x_2$, then eq. (2) becomes a first-order, forward and backward, finite-difference approximations of the slowness u respectively, as follows

$$\underbrace{u(x_0 = x_1) = \frac{t_1 - t_2}{d_1 - d_2} + O(\Delta d)}_{\text{forward approximation}}, \quad \underbrace{u(x_0 = x_2) = \frac{t_2 - t_1}{d_1 - d_2} + O(\Delta d)}_{\text{backward approximation}}. \quad (3)$$

Note that we have assumed that $d_2 > d_1$. On the contrary, if one assumes that x_0 is the middle point between x_1 and x_2 , then eq. (2) becomes a second-order centered finite difference approximation of the slowness u , as follows

$$\underbrace{u(x_0 = (x_1 + x_2)/2) = \frac{t_1 - t_2}{\Delta d} + O(\Delta d^2)}_{\text{centered approximation}}, \quad (4)$$

which means that the slowness evaluated at the center point x_0 between x_1, x_2 can be approximated (up to second-order accuracy) by dividing the arrival travel time of the wave of interest and the difference between epicentral distance of the stations (see Fig. 1-b and Fig. 1-c).

Equation (4) brings a different physical interpretation since in fact, we are not measuring travel-times at the center of the two stations. We, however, are computing a second-order approximation to a slowness value located at the *virtual receiver* located at the middle between the two stations.

If we consider the calculation of the slowness in a spherical Earth, we can write the velocity of the medium at the deepest point of the ray v_d as follows (Rost and Thomas, 2002)

$$v_d = \frac{1}{u} \frac{r_d}{r_{\text{earth}}} \quad (5)$$

where r_{earth} is the radius of the Earth, and r_d is the radius r of the turning (deepest) point of the (non bouncing) ray.

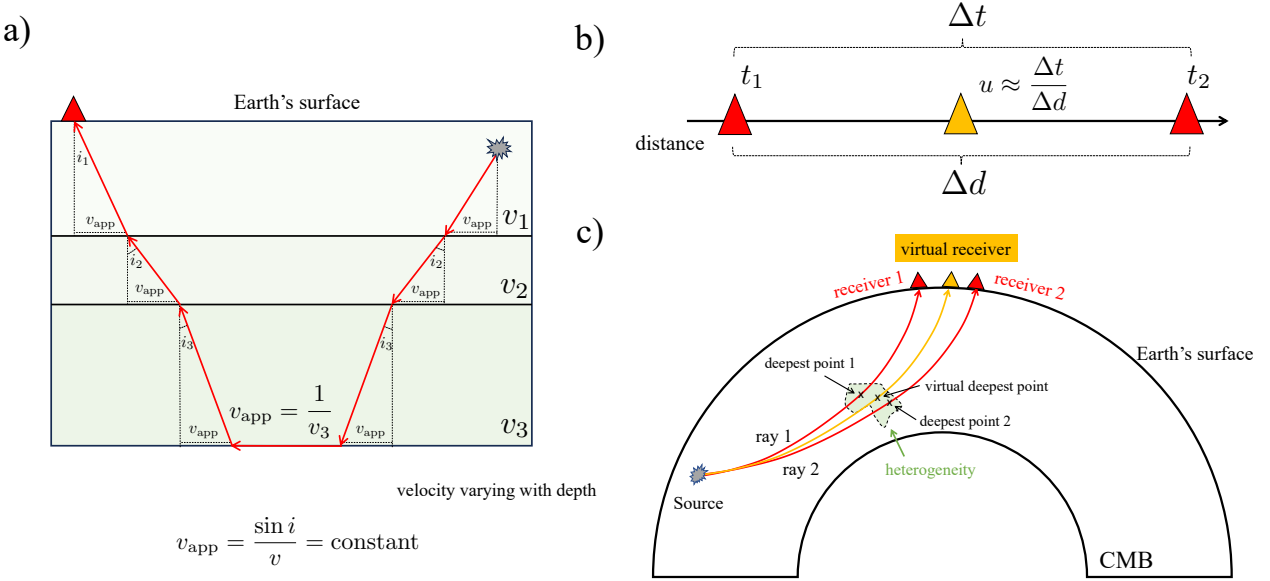


Figure 1: a) Ray theory in a layered medium. b) Second-order finite-difference slowness approximation. c) The virtual receiver approach methodology proposed in this study.

3 Validation

3.1 Theory

We validate the accuracy of eq. (4), for which we will assume, like in the rest of the paper, that x_0 is the middle location between x_1 and x_2 . We assume that the observed slowness (u^{observed}) can be written as the predicted slowness using certain earth model (u^{model}) plus a slowness perturbation/deviation (δu) as follows

$$\begin{aligned} u^{\text{observed}}(x_0) &= u^{\text{model}}(x_0) + \delta u, \\ &\approx \frac{\Delta t^{\text{observed}}}{\Delta d}, \\ &\approx u^{\text{model}}(x_0) + \frac{\Delta t_2 - \Delta t_1}{\Delta d}, \end{aligned} \quad (6)$$

where we have used the notation $(\Delta t_1, \Delta t_2) = \Delta t_{1,2}$ and with $\Delta t_{1,2} = t_{1,2}^{\text{observed}} - t_{1,2}^{\text{model}}$.

Note that the slowness variation δu is simply given by the difference time anomalies $\Delta t_1, \Delta t_2$ measured at the two stations and divided by Δd , that is,

$$\delta u = \frac{\Delta t_1 - \Delta t_2}{\Delta d}. \quad (7)$$

Equation (7) means that any error in the slowness calculations will arise from travel time measurements only. If we assume a linear dependence between the model and observations we can write observed travel times ($t_{1,2}^{\text{observed}}$) as follows

$$t_{1,2}^{\text{observed}} = \alpha_{1,2} t_{1,2}^{\text{model}}, \quad \text{with } \alpha_{1,2} \in \mathbb{R}, \quad (8)$$

which leads to

$$\Delta t_{1,2}(x_0) = t_{1,2}^{\text{model}} - t_{1,2}^{\text{observed}} = (1 - \alpha_{1,2}) t_{1,2}^{\text{model}}, \quad \text{with } \alpha_{1,2} \in \mathbb{R}, \quad (9)$$

where $\alpha_{1,2}$ are non-dimensional real parameters. Equation (9) implies that both rays should see the same (anomalous) structure (see Fig. 1–c, otherwise we will not be able to correctly image a structure). This means that the non-dimensional

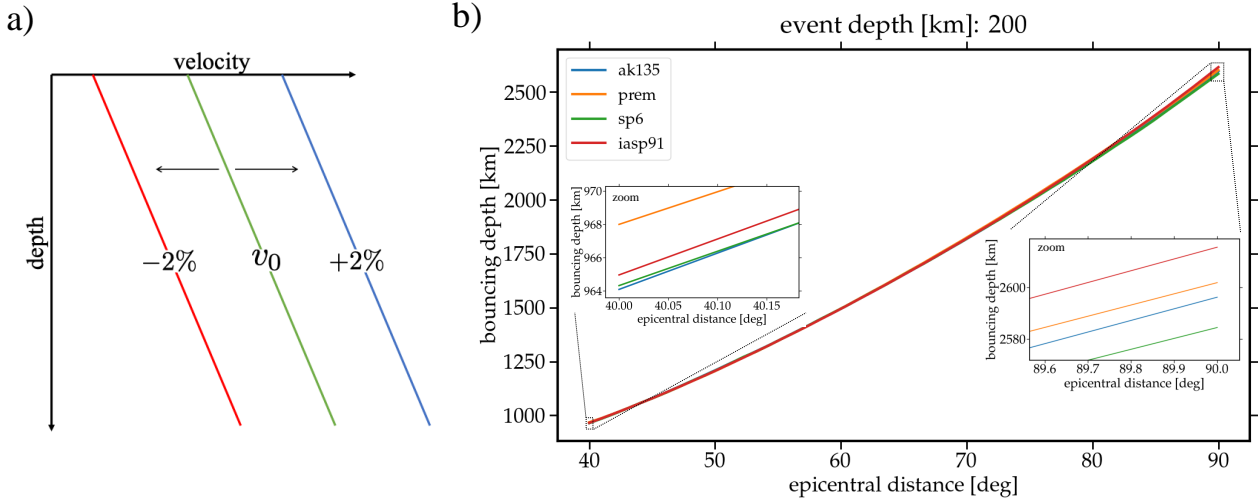


Figure 2: a) Illustration of a 1D model v_0 and its corresponding predicted models for a relative slowness calculations of $\pm 2\%$ predicted using eq. (4). b) Bouncing depth (deepest point) of the S wave predicted by different tomographic models.

parameters ($\alpha_{1,2}$) should be the same at both receivers, i.e., $\alpha_1 = \alpha_2 = \alpha$. We thus can write eq. (6) as follows

$$u^{\text{observed}}(x_0) \approx \frac{\Delta t^{\text{observed}}}{\Delta d} = \frac{t_2^{\text{model}} - t_1^{\text{model}}}{\Delta d} (1 - \alpha). \quad (10)$$

In practice, however, $\alpha_1 \neq \alpha_2$ and therefore we must allow some error (ε), i.e.,

$$|\alpha_1 - \alpha_2| < \varepsilon, \quad \text{with } \varepsilon \in \mathbb{R}^+. \quad (11)$$

3.2 Numerical results

For travel time and slowness calculations we use the TauP toolkit (Crotwell et al., 1999) implemented in Obspy (Krischer et al., 2015).

What does a velocity perturbation of X% mean?: The approximation of the slowness given by eq. (4) suggests that any travel time perturbation α will make a change in the slowness prediction. This means that any change in the slowness will be mapped into the whole initial velocity model assumed. In other words, any 1D or 2D initial model will be equally perturbed in its totality (see Fig. 2-a).

Depth predictions: Absolute velocity predictions obtained using eq. 4 are independent of the earth model assumed. However, to locate/assign the deepest point of the ray (bounding location) we need to assume an earth model. Different 1D tomographic models can be used for this purpose. To develop intuition on the different depth obtained we assume a 200 km deep event and four different tomographic models: PREM (Dziewonski and Anderson, 1981), AK135 (Kennett et al., 1995), SP6 (Morelli and Dziewonski, 1993) and IASP91 (Kennett and Engdahl, 1991). Different bouncing point for S waves are presented in Fig. 2-b, where we can observe that at short distances ($\sim 40^\circ$) the maximum differences between in the depths predictions is ~ 4 km, and a larger distances ($\sim 90^\circ$) the maximum differences between in the depth predictions is ~ 30 km.

For the rest of the calculations we will assume the earth model PREM (Dziewonski and Anderson, 1981). Assuming any other earth model will lead to the same analysis presented next.

The sensitivity to station-to-station distance: To evaluate the influence of station-to-station distance in slowness calculations using eq. (4), we first assume an event at 500 km depth and a first station located at 70° epicentral distance. We next vary the epicentral distance of the second station between $[0.001^\circ, 15^\circ]$. Results are presented in Fig. 3-a, were

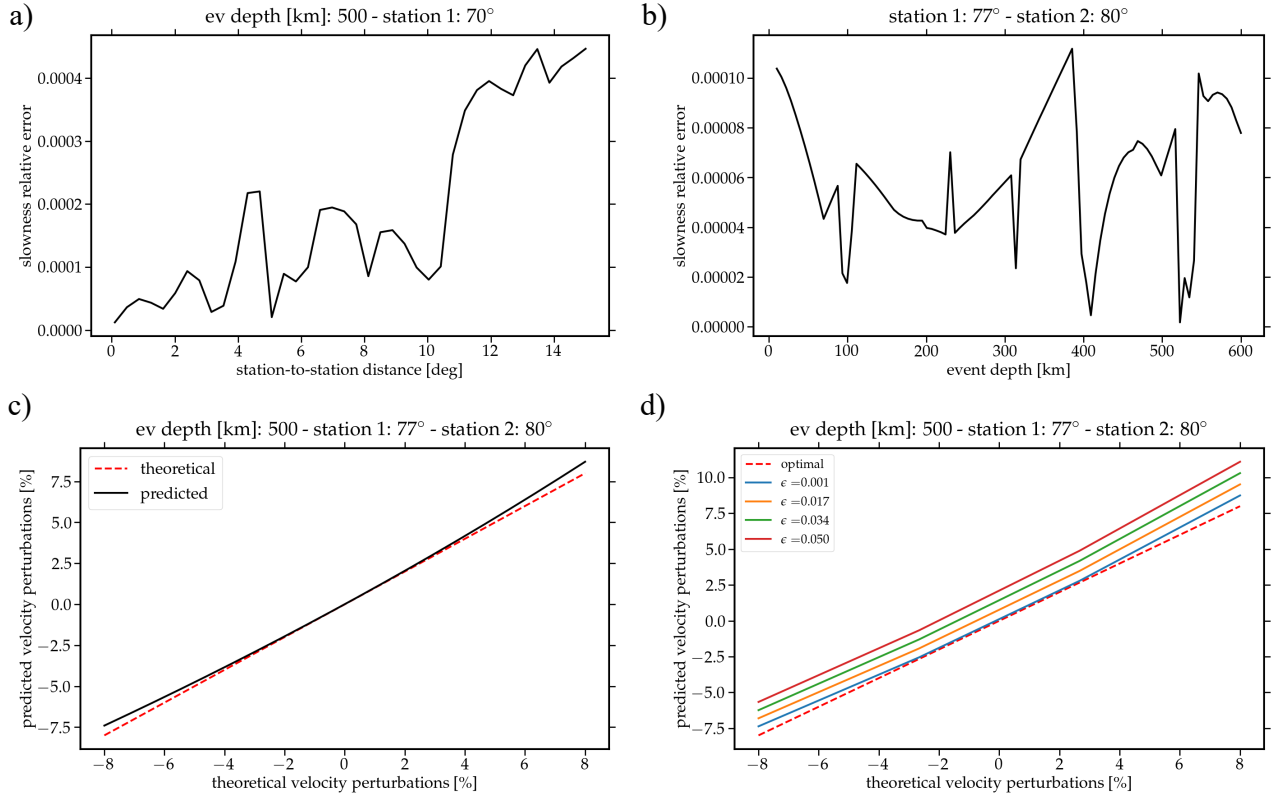


Figure 3: Methodology validation.

we can observe that the relative error is smaller than 0.0004 for station-to-station distance smaller than fifteen degrees. These are unexpected results since at distances larger than two degrees one can, intuitively, expect the approximation to break-down.

The sensitivity to the event depth: Having validated the sensitivity to station-to-station distance, we now evaluate the sensitivity to the event depth. We select two stations at 77° and 80° , i.e., separated by three degrees. We select three degrees as the largest distance that one can intuitively apply eq. (4). Results are presented in Fig. 3-b, were we can observe that the relative errors are always smaller than 0.0001. It thus seems that the approximation made in eq. (4) is also insensitive to the event depth.

The sensitivity to velocity perturbations: We can evaluate a velocity perturbation as seen by the slowness by simply adding travel-time perturbations to eq. (10) using a single α parameter. This means that we are assuming that both recorded travel times (t_1, t_2) see exactly the same anomaly perturbation. Results are presented in Fig. 3-c, where we can observe that predictions are accurate up to $\sim \pm 3\%$. This result is consistent and expected due to limitations of the approximations made by ray theory. We thus cannot expect to realistically obtain/interpret velocity perturbations larger than $\sim \pm 3\%$.

The sensitivity to ϵ (eq. (11)): In realistic scenarios, when evaluating eq. (9), we should expect that $\alpha_1 \neq \alpha_2$. These parameters give information about the heterogeneities that both rays are crossing: If $\alpha_1 = \alpha_2 = \alpha$, then it is guaranteed that both rays see the same structure. In realistic scenarios, on the contrary, we must allow some error ϵ (see eq. (11)).

We next evaluate the magnitude of the error ϵ in eq. (11) for different velocity perturbations. Results are presented in Fig. 3-d, where we can observe that predictions are highly sensitive to small perturbations of ϵ . These results suggest that in order to have consistent predictions $\sim \pm 3\%$, we should set $\epsilon \leq 0.001$.

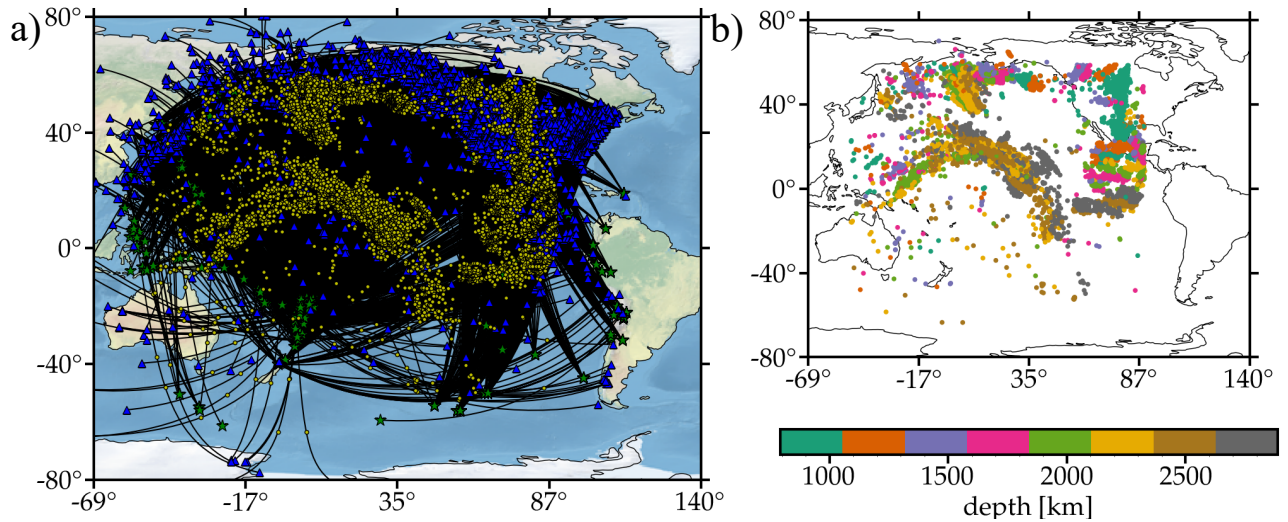


Figure 4: a) Ray paths, stations in blue triangles, events in green stars and the turning point of the ray in yellow circles. b) Depth of the turning point of the rays.

4 Application to seismological observations

4.1 Data set

We use the travel-time database provided by [Lai et al. \(2019\)](#), which provides travel times of transversely polarized SH waves on a global scale obtained from an adaptive empirical wavelet construction technique. We, however, focus on events for which the deepest point of the S wave is located in the circum-pacific region. Fig. 4-a shows the ray paths that sample the area of interest. From the selected sub-data set we apply the virtual receiver methodology previously presented.

Errors: We allow a maximum distance between stations of ~ 1.5 degree (~ 150) km, and an error $\varepsilon < 0.00005$ (see eq. (11)) which guarantees that the velocity anomaly that both stations see is have the same magnitude (which we interpret as the same structure). Travel time measurements errors coming from [Lai et al. \(2019\)](#) do not significantly affect our results, since travel time errors are around ~ 1 s. To gain some intuition on how an error of ± 1 s affects our results, consider an event of 500 km depth and recorded at a distance of 78° . The predicted S travel time obtained using the Obspy Taup toolkit ([Crotwell et al., 1999](#); [Krischer et al., 2015](#)) and assuming PREM as the background earth model, is of 1217.8 s. Thus, the error of ± 1 s represents approximately the $\pm 0.08\%$ of the final slowness/velocity prediction (see (10)).

4.2 Results

We obtained a total of 14686 local-velocity measurements, spanning depths from 792.6 km to 2888.8 km, sampling the entire lower mantle from top to bottom (see Fig. 4-b). We emphasize that the spatial distribution of the results depends on the locations of the events and stations. The results obtained are not intended to produce an image but rather to sample the data points directly, which we chose not to interpolate. While transforming these points into an image might seem useful, doing so would compromise the integrity of the discrete data. Hence, we refer to the map view at different locations.

Statistics: The shear wave velocity values estimated range from 6.178 km/s to 7.382 km/s with a mean value 6.951 km/s and a median of 7.052 km/s (see Fig. 5). Overall, these align well with the velocity gradients predicted by PREM ([Dziewonski and Anderson, 1981](#)), as shown in Fig. 5.

We next normalize all velocity values obtained with respect to PREM. As a result, and generally speaking, most of our sampled points exhibit velocity anomalies between -1% and $+1\%$ (see Fig. 5). Larger anomalies ($> |1\%|$) are predominantly found below 2250 km depth. Out of our dataset, 7693 sample points lie between this depth and the CMB,

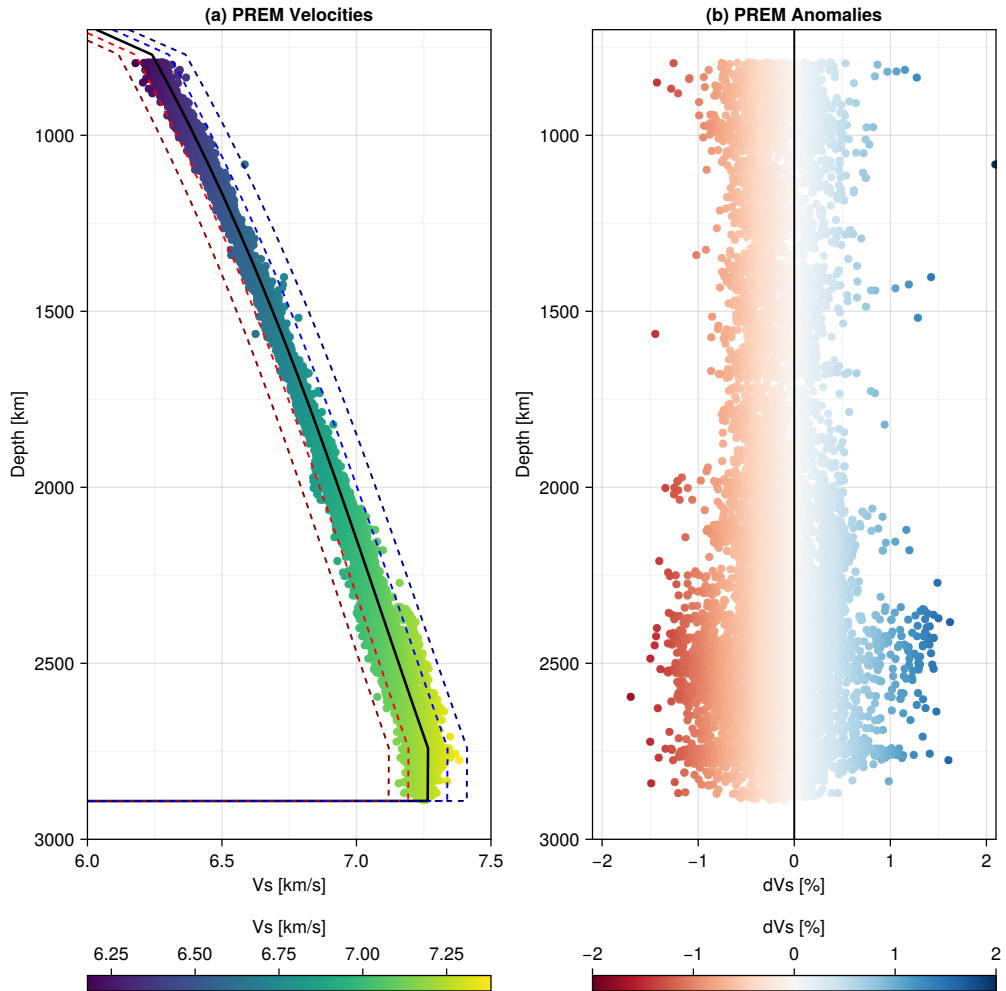


Figure 5: a) Shear wave velocity values estimated using the VRA and compared to PREM b) Normalized shear wave velocity values (with respect to PREM) estimated using the VRA.

with anomalies ranging from -1.702% to 1.621%. The mean and median values for this range are -0.187% and -0.197%, respectively, again highlighting the prevalence of negative anomalies in the dataset and, consequently, in the lower mantle beneath the Pacific Ocean, which is largely related to the Pacific LLSVP (Garnero and McNamara, 2008; Schubert et al., 2004; McNamara, 2019). At this depth range, 2233 sampling points show positive anomalies, while 5460 exhibit negative ones. Positive anomalies, which are a statistical minority in the dataset (2233 out of 7693 points), stand out within the predominantly well-known negative anomaly environment of the LLSVP. The negative anomalies exhibit a mean value of -0.388% and a median value of -0.339%, indicating that the data is clustered around its central tendency, a behavior characteristic of a normal or near-Gaussian distribution. This statistical stability reflects the dominance of low-velocity anomalies within the LLSVP. In contrast, the positive anomalies deviate from this pattern, with a mean of 0.306% and a median of 0.213%, showing a noticeable gap between them. This suggests a more skewed distribution or irregular behavior.

Comparisons against tomographic models: We next compare velocity predictions against two different tomographic models built with different techniques and datasets: (i) SEMUCB-WM1 (French and Romanowicz, 2014), built with full-waveform inversion techniques and SEISGLOB2 (Durand et al., 2017), built using ray theory and normal modes.

We analyze three different depths: 2600 km, 2700 km and 2800 km. For each depth, we gather our predictions within a depth range of 100 km. This means, for example, that we compare the tomographic image at 2600 km against out observations that lay between 2550–2650 km depth range. This depth range seems good enough to cover the depth uncertainty of our predictions close to the CMB (see Fig. 2–b). Results are presents in Fig. 6, where we can observe three main features: (i) the Galapagos plume, (ii) the LLSVP boundary and (iii) high-velocity anomalies inside the LLSVP.

We further project the data close to the Hawaiian and Galapagos archipelagos into two profiles: profile H-H' and profile G-G', respectively (see Fig. 7). The VRA samples in a 10° corridor are projected into each profile and we plot them in top of an average tomography tomography model (see Fig. 7-a and -b). Six S wave tomography models, downloaded from the SubMachine database (Hosseini et al., 2018), are averaged: French and Romanowicz (2014); Moulik and Ekström (2014); Lu and Grand (2016); Koolemeijer et al. (2016); Lu et al. (2019); Tesoniero et al. (2015). These are selected as the present good resolving power around the target profile. In the profiles the signature low velocity anomaly of the Pacific LLSVP/Hawaiian plume (see Fig. 7-a) and the Galapagos plume (see Fig. 7-b) are clearly imaged by tomographic techniques. The location of the low velocity VRA samples clearly correlates with both structures. High velocity points in the H-H' profile are fairly abundant and clustered while there tend to be more spare and less in number in the G-G' profile.

5 Discussion

The deep roots of the Galapagos plume The Galapagos plume is located above the eastern margin of the Pacific LLSVP and it has its seismic signature has been reported in the literature (e.g. Cottaar et al., 2022; Villagómez et al., 2014; Nolet et al., 2019; Harpp and Weis, 2020). Our observations show that the slowest velocity areas are located beneath the Galapagos, which is in agreement with the presence of the plume in the lower-most mantle. However, we are not able to detect the previously reported mega-ULVZ (e.g. Cottaar et al., 2022; Vanacore and Niu, 2011). This may be explained by two reasons: (i) due to the location of the bounce points and/or (ii) that due to the limitations in our methodology presented in Fig. 3–c, we are able to properly image up to $\pm 3\%$ of velocity perturbations. Different than those values, the ray theory approximations break down leading to an underestimation of the velocity values. As a consequence, extreme velocity reductions produced by ULVZs may be misinterpreted as simple low velocity zones as represented in the profile G-G' in Fig. 7.

In general terms, high velocity VRA samples close and around the Galapagos plume show shear wave anomalies close to zero ($0.0\% < dVs < 0.25\%$). These values do not necessarily indicate, as we will pose later large variations in the chemical or thermal structure of the plume. We propose they are related to the complexity of the convection system around the plume in which the mantle can be trapped/dragged/mixed in the spreading and upwelling of the plume's material.

High-velocity anomalies inside LLSVP? Compositional interpretation Silicate perovskite ($(\text{Mg},\text{Fe})\text{SiO}_3$) is one of the most abundant materials in the planet, and it is primarily found in the lower mantle, between approximately 660 km and the CMB (Tsuchiya et al., 2004; Murakami et al., 2012). It undergoes a phase transition (structural rearrangement) to post-perovskite at pressures greater than ~ 125 GPa that corresponds to depths between 2700 km and the CMB and it

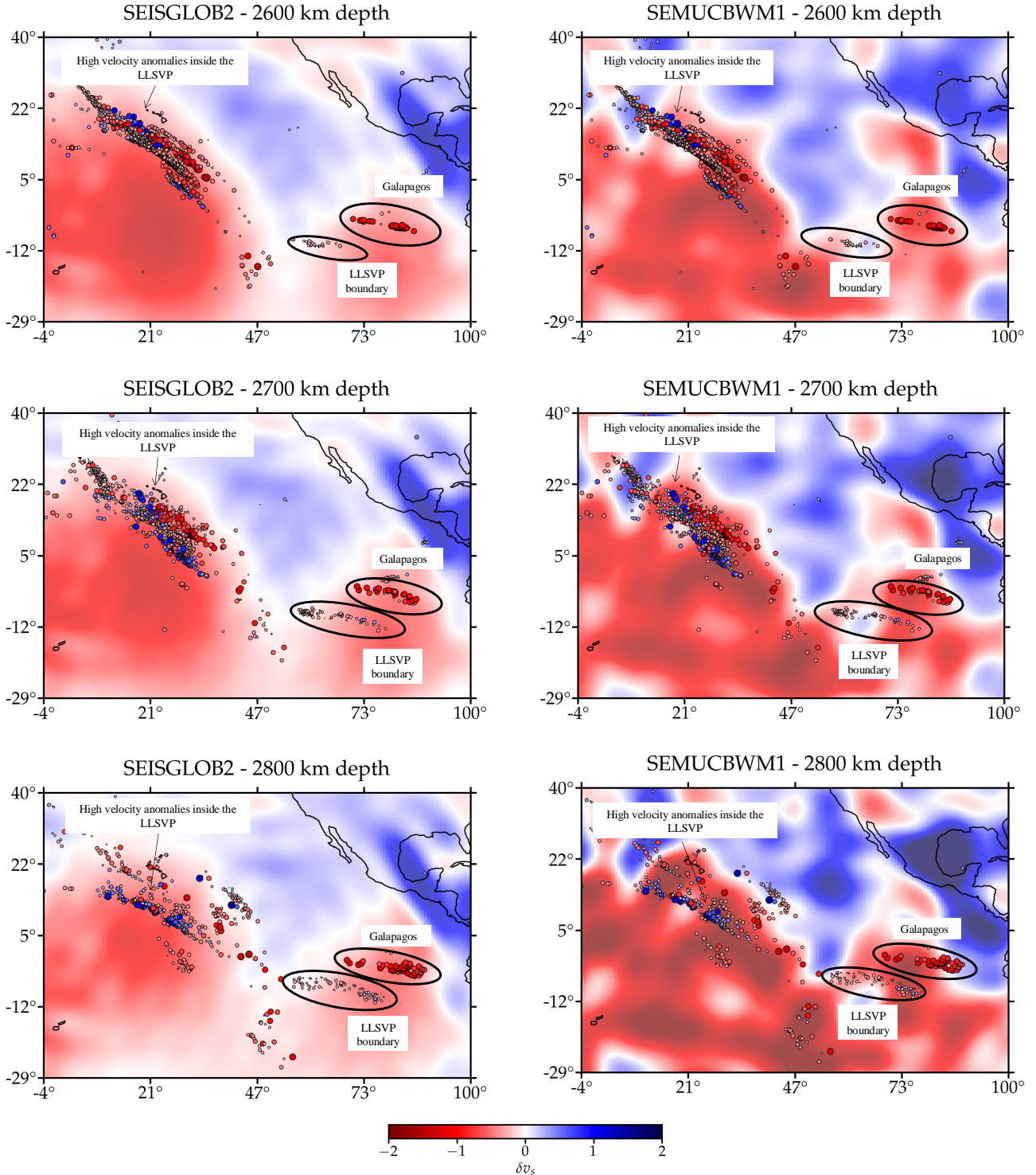


Figure 6: Results obtained using the virtual receiver methodology compared against tomographic models sat different depths. For clarity, the size of the velocity anomalies computed (circles) are scaled to their magnitudes.

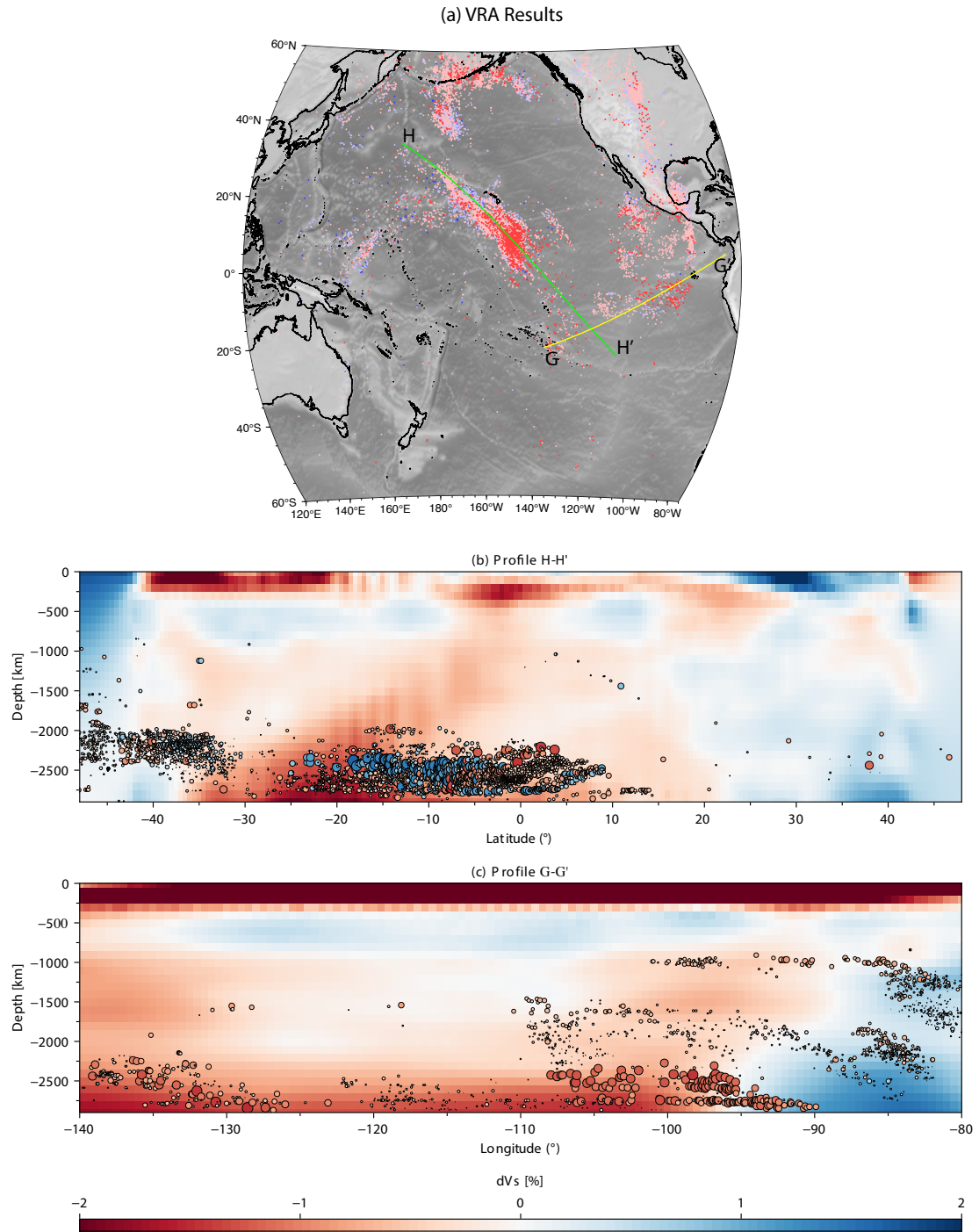


Figure 7: a) Location of the Depth of the turning point of the rays and their corresponding velocity perturbations obtained using the VRA. b) Vertical profile crossing the Pacific LLSVP and c) vertical profile crossing the Galapagos plume. For clarity, the size of the velocity anomalies computed (circles) are scaled to their magnitudes.

is usually correlated to the D'' layer (e.g. Oganov and Ono, 2004; Murakami et al., 2004; Hirose et al., 2013; Murakami et al., 2012; Shim et al., 2007; Williams et al., 1987; Shim, 2008; Tateno et al., 2009; Tsuchiya and Tsuchiya, 2006).

The perovskite-to-post-perovskite transition is critical for understanding the seismic discontinuity observed in the D'' layer. Theoretical and observational studies report that the phase transition to post-perovskite produces a positive jump in shear wave velocity (+dVs) (Wookey et al., 2005; Stackhouse et al., 2006; Tsuchiya and Tsuchiya, 2006; Wentzcovitch et al., 2006; Oganov and Ono, 2004; Garnero and McNamara, 2008; Deschamps et al., 2012; Vilella et al., 2021; Murakami et al., 2012; Hirose et al., 2013).

Our observations reveal high-velocity anomalies inside the Pacific LLSVP (see Figs. 6). High-velocity regions in the lower mantle have been previously reported (Dziewonski et al., 1977; Jordan and Lynn, 1974), with most of these associated with long-lived subduction slabs (Suzuki et al., 2020). It has been proposed (e.g. Tackley, 1998) that D'' in the LLSVP beneath the Pacific is chemically distinct from D'' in other regions due to dense debris of subducted oceanic slabs, possibly dating back to the formation of the Rodinia supercontinent (Maruyama et al., 2007a). Additionally, remnants of mid-ocean ridge basalt (MORB) crust are expected to have accumulated in the D'' beneath the Pacific (e.g. Christensen and Hofmann, 1994).

It is possible to interpret the shear wave velocity values recovered from the VRA below 2250 km depth in petrochemical terms to a certain extent. One effective approach involves estimating Vs for a range of petrological compositions (C) while accounting for in-situ temperature (T) and pressure (P) conditions at depth. Similar methodologies have been employed to investigate compositional and thermal variations within the crust and mantle (e.g. Khan et al., 2009; Müntener and Ulmer, 2018; Fullea et al., 2021).

We here use the SEITCOMP V1.0 code (Arnaiz-Rodriguez and Fullea, in preparation). In general terms, T is derived by solving the heat equation in 1D from the CMB to the surface, considering depth-dependent variations in density (automatically derived from a reference composition C_0), heat capacity, thermal conductivity, and radiogenic heat production. The in-situ pressure (P) values are calculated based on the density model and align closely with those reported in PREM. The mantle composition (C) is parameterized using stable mantle mineral assemblages, modeled through Gibbs free energy minimization schemes assuming thermodynamic equilibrium ($T > 500^\circ\text{C}$) (e.g. Connolly, 2005). A standard characterization of mantle composition is based on the main major oxides in the CFMAS system (CaO–FeO–MgO–Al₂O₃–SiO₂) (e.g. Harley, 1984; Nakagawa et al., 2010, 2009). To simplify the composition C, SEITCOMP adopts the discretisation of Fullea et al. (2021) where the wt% amounts Al₂O₃ and FeO oxides in the mantle layers are free variables, and CaO–MgO amounts are statistically correlated to Al₂O₃ (e.g. Afonso et al., 2013).

Therefore, at each VRA sample, we use the estimated values of temperature (T) and pressure (P) and define the composition (C) as a combination of Al₂O₃ and FeO values. In general terms, Al₂O₃ concentration is expected to range from 1.0 wt% to 6.0 wt%, while FeO typically ranges between 7.0 wt% and 10 wt%. As reference values, the original or primitive mantle composition is assumed to contain approximately 3.6 wt% Al₂O₃ and 8.0 wt% FeO (e.g. McDonough and Sun, 1995), while the theoretical rock pyrolite has a composition of 3.98 wt% Al₂O₃ and 8.18 wt% FeO (e.g. Workman and Hart, 2005).

It is worth noting that in LLSVPs, larger compositional ranges may be necessary to explain the observed rock properties (e.g. Vilella et al., 2021). For this study, we set Al₂O₃ to vary from 1 wt% to 11 wt%, while FeO varies from 1 wt% to 20 wt%. Then, for each sample, we calculate the Vs value across all possible combinations of Al₂O₃ and FeO at 0.1 wt% intervals, considering pressure and temperature at the corresponding depth. This method produces an iso-Vs line or contour (see Fig. 8).

In Fig. 8, all iso-Vs lines are plotted together to interpret the reported shear-wave velocities. We divide the data into six ranges:

- $0.0\% < |dVs| < 0.5\%$
- $0.5\% < |dVs| < 1.0\%$
- $1.0\% < |dVs| < 2.0\%$

At a first glance, the wt% of FeO clearly dominates the shear-wave velocity variations in the lower mantle. Higher FeO concentrations correlate with negative shear-wave velocity anomalies, while lower concentrations correlate with positive ones. This trend is consistent for samples at the top of the section (lower Vs, represented by purple lines) and for values closer to the CMB (higher Vs, represented by green and yellow lines).

Small velocity anomalies ($0.0\% < |dVs| < 0.5\%$) at the top of the section ($z < 2500$ km) can be relatively well linked to moderate variations in FeO content. We observe that these anomalies are well explained by FeO concentrations ranging between 8.0 and 10.7 wt%, which fall within the expected ranges for typical primordial or fertile mantle with a

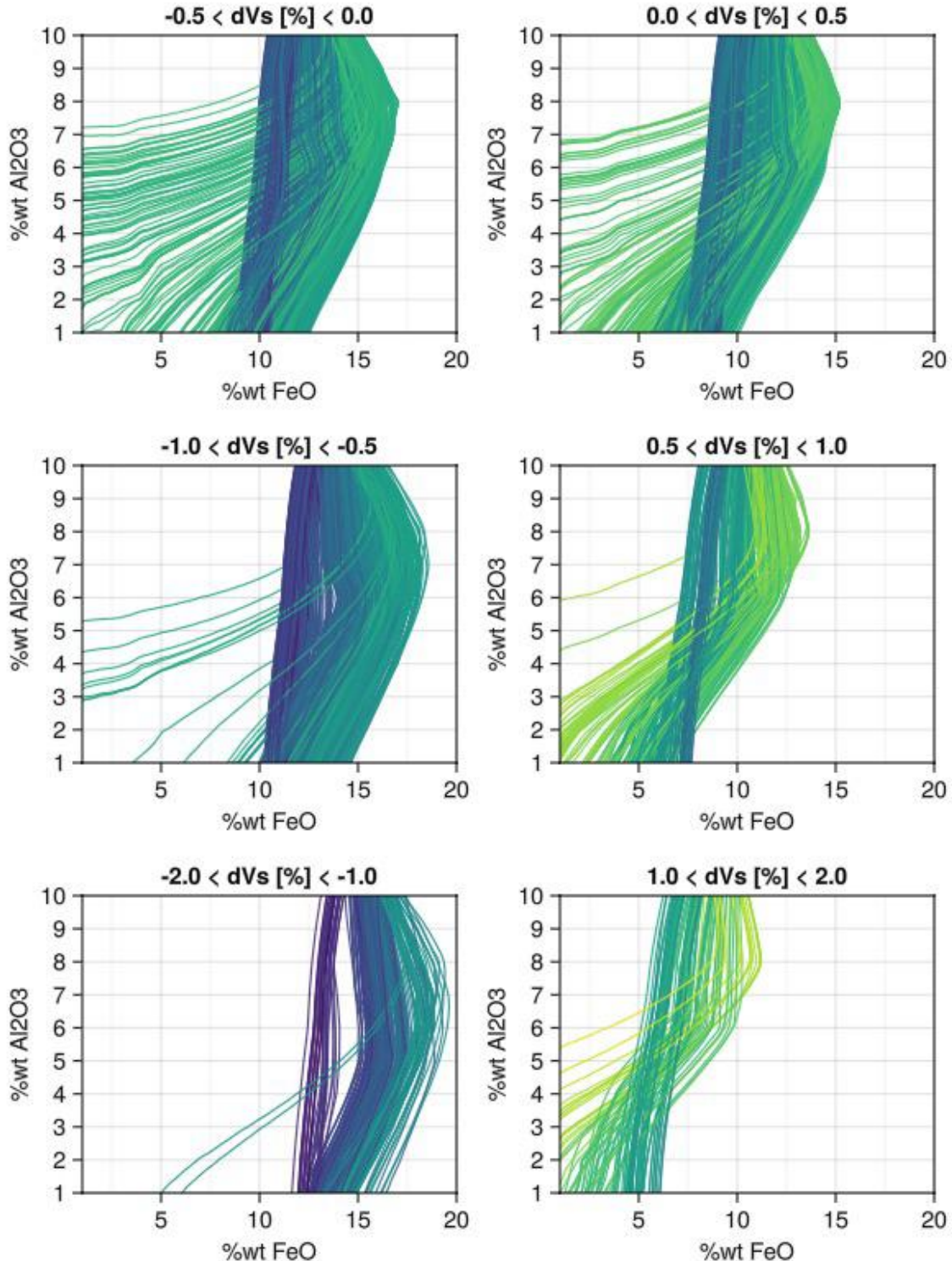


Figure 8: Compositional results obtained using the SEITCOMP code.

perovskite-dominated composition (~ 8 – 10 wt%) (e.g. Palme and O’Neill, 2007; Fei et al., 1996). At this depth range, intermediate anomalies ($0.5\% < |dVs| < 1.0\%$) require larger variations in FeO. Negative anomalies are consistent with FeO concentrations of approximately 12 wt%, possibly indicating the existence of some *basaltic material*, that is, a fine-scale mélange predominantly composed of mafic mantle rocks, such as high-pressure polymorphs of Mid-Ocean Ridge Basalt (MORB), with some contribution from FeO rich ultramafic rocks, like lherzolite or harzburgite (e.g. Ballmer et al., 2016b). Positive anomalies align with lower FeO concentrations around 7.5 wt%, which could be associated with depleted mantle—potentially residues of melting processes (e.g. Workman and Hart, 2005).

Larger velocity anomalies ($1.0\% < |dVs| < 2.0\%$) require significantly anomalous FeO content to be explained. Negative anomalies suggest FeO concentrations around 13 wt%, while positive anomalies correspond to FeO levels of about 5.1 wt%. These extreme positive anomalies might indicate the presence of post-perovskite-type material in the lower mantle, as FeO content in post-perovskite is expected to be lower (5–8 wt%) compared to perovskite (6–10 wt%) (e.g. Simmyo et al., 2008; Dorfman and Duffy, 2014; Tateno et al., 2007).

Finally, at the bottom of our study region, i.e., depths larger than 2500 km up to the CMB, there is no clear FeO value to account for small velocity anomalies ($0.0\% < |dVs| < 0.5\%$). While the trend connecting shear wave velocity (Vs) with FeO wt% observed earlier persists, no large variations are observed around a mean value of 12.5 wt%. Larger variations are found in mid-range ($0.5\% < |dVs| < 1.0\%$) and large ($1.0\% < |dVs| < 2.0\%$) anomalies, with an average FeO content of 15 wt% for positive anomalies and 5 wt% for negative anomalies.

It is evident, assuming that temperature variations due to internal convection within the LLSVP system do not contribute significantly to Vs variations, that we are likely dealing with two distinct mantle phases: one characterized by negative Vs anomalies and high FeO content, and the other by positive Vs anomalies and lower FeO content. For the first phase, previous studies (e.g. Vilella et al., 2021) have suggested that LLSVPs might have a high density (consistent with large FeO content), which could stabilize them against the more vigorous mantle convection, thereby giving them their characteristic low Vs. Our observed values align with this interpretation. Additionally, negative anomalies are statistically dominant in our sampled points, which reflects the general composition of the Pacific LLSVP.

As for the second phase, the high-velocity, low-FeO content post-perovskite material abundant in the lowermost mantle is a likely candidate to explain the positive anomalies within the LLSVP. The exact geographical location and nature (thermal or thermochemical) of the Pacific LLSVP edges are not well constrained or understood (see McNamara (2019) for a recent review). If the Pacific LLSVP represents hotter regions of the mantle, perovskite is expected to dominate the mineralogical composition, depending on pressure and the amount of iron and alumina, due to the positive Clapeyron slope of the perovskite-post-perovskite system (Oganov and Ono, 2004; Tsuchiya et al., 2004; Catalli et al., 2009; Hernlund et al., 2005; Sun et al., 2018; Vilella et al., 2021).

Because there positive and negative anomalies samples are at a close distance (sometimes smaller than one degree; see Fig. 6), there must be a lateral transition from perovskite to postperovskite inside the LLSVP. This phenomenon may occur somewhere close to the border of the LLSVP, across a few hundred km (<200 km) wide zone (see Fig. 9). These high velocity observations inside the LLSVP seem to be compatible with previous studies (e.g. Deschamps et al., 2012; Vilella et al., 2021), supporting the idea that the Pacific LLSVP may have a different mantle composition that perturbs the phase boundary depth. Therefore, during the formation and ongoing convective evolution of the LLSVPs, some post-perovskite material may have been incorporated into the LLSVPs. This could potentially mix with the surrounding material, creating small regions with moderate to high positive anomalies within a larger negative-anomaly region. This interpretation is consistent with convective models of LLSVP evolution, in which LLSVP material mixes with lower mantle material (e.g. Ballmer et al., 2016a). These small and sparse regions would be hard to detect when averaging the travel time information (like in tomography studies) but easily detected when sampling the lower mantle with more delicacy. Hence, we propose that they can be better assessed by accounting for the shear wave variations here reported.

Finally, although our results are compatible with the inclusion of high-velocity post-perovskite phases into the LLSPV province, we cannot differentiate between this material and basaltic mantle that may accumulate in the lower mantle from ancient subductions (e.g. Christensen and Hofmann, 1994). Generally speaking, one would not expect this kind of structure to be in the middle of the Pacific ocean, away from subduction zones, but recently an stagnant slab has been discovered on the Southern Pacific beneath the East Pacific Rise (Wang et al., 2024) opening a different explanation to our results. If an ancient slab had reached the mantle, perhaps before the Triassic (as per Wang et al. (2024) calculations), its basaltic material may have mixed within the Pacific LLSVP creating chemically anomalous regions within it.

The Virtual Receiver Methodology: Further Developments We have developed a new imaging technique based on the calculation of slowness using a pair of stations. Based in this result, and the fact that the phase velocity is equal to the medium velocity at the turning point of waves that do not reflect at any boundary, we are able to image any (slowly

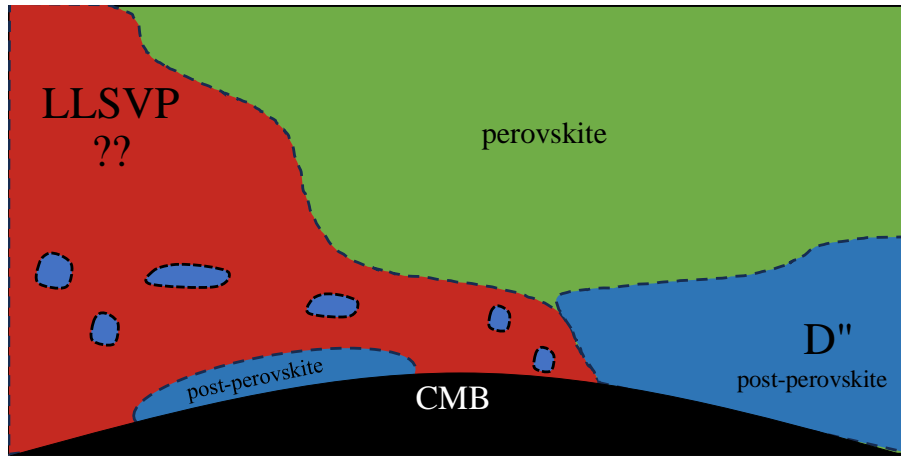


Figure 9: Schematic representation of the presence of post-perovskite inside the Pacific LLSVP.

varying in velocity) structure.

For slowness calculations, we have assumed an isotropic medium, allowing us to place any pair of receivers in any directions. Anisotropic imaging, like for instance transverse isotropy, can in principle be achieved by simply analyzing SH and SV travel times independently.

Slowness calculations can, additionally, be performed in several ways: (i) using seismic arrays (e.g. [Rost and Thomas, 2002](#); [Métaxian et al., 2002](#)) and, more recently, (ii) using a pair of translational and rotational stations (e.g. [Igel et al., 2021](#); [Fichtner and Igel, 2009](#); [Bernauer et al., 2020, 2012](#); [Trifunac, 2006](#); [Bernauer et al., 2009, 2014](#); [Reinwald et al., 2016](#); [Abreu et al., 2023](#)).

6 Conclusions

In this study we present novel results that provide new insights into the internal composition/dynamics of the Pacific LLSVP. We developed and employed the Virtual Receiver Approach (VRA) to directly estimate shear-wave velocities in the lower mantle. Our findings reveal a more complex internal structure than previously reported, characterized by zones of high-velocity anomalies within the Pacific LLSVP. These, challenge the traditional conscript of LLSVPs as homogeneous low-velocity regions and suggest significant lateral thermo-chemical heterogeneity.

The observed high-velocity anomalies are consistent with low FeO compositions, indicating the potential presence of post-perovskite (or other dense, Fe-depleted phases) possibly resulting from the interaction of the LLSVP and the mantle convection. Another possible explanation is the incorporation of subducted basaltic material into the Pacific LLSVP by an hypothetical ancient subducting slab. Conversely, low-velocity anomalies align with FeO-rich compositions, supporting the hypothesis of LLSVPs as thermo-chemical dynamic structures composed of dense primordial mantle components.

These observations advance our understanding of LLSVPs as dynamic, thermo-chemically diverse structures, with implications for mantle convection, plume generation, and core-mantle heat transfer. Future work integrating high-resolution imaging techniques and petrological modeling is essential to refine our understanding of the role of LLSVPs in Earth's geodynamic processes.

7 Acknowledgments

RA acknowledges the fruitful conversations with Saksham Rohilla and the seismology group of the University of Münster.

References

- Abreu, R., Durand, S., Rost, S., and Thomas, C. (2023). Deep earth rotational seismology. *Geophysical Journal International*, 234(3):2365–2374.

- Afonso, J. C., Fullea, J., Yang, Y., Connolly, J., and Jones, A. (2013). 3-D multi-observable probabilistic inversion for the compositional and thermal structure of the lithosphere and upper mantle. II: General methodology and resolution analysis. *Journal of Geophysical Research: Solid Earth*, 118(4):1650–1676.
- Aki, K., Christoffersson, A., and Husebye, E. S. (1977). Determination of the three-dimensional seismic structure of the lithosphere. *Journal of Geophysical Research*, 82(2):277–296.
- Avants, M., Lay, T., Russell, S. A., and Garnero, E. J. (2006). Shear velocity variation within the D'' region beneath the central Pacific. *Journal of Geophysical Research: Solid Earth*, 111(B5).
- Ballmer, M. D., Schumacher, L., Lekic, V., Thomas, C., and Ito, G. (2016a). Compositional layering within the large low shear-wave velocity provinces in the lower mantle. *Geochemistry, Geophysics, Geosystems*, 17(12):5056–5077.
- Ballmer, M. D., Schumacher, L., Lekic, V., Thomas, C., and Ito, G. (2016b). Compositional layering within the large low shear-wave velocity provinces in the lower mantle. *Geochemistry, Geophysics, Geosystems*, 17(12):5056–5077.
- Bernauer, F., Wassermann, J., and Igel, H. (2020). Dynamic tilt correction using direct rotational motion measurements. *Seismological Society of America*, 91(5):2872–2880.
- Bernauer, M., Fichtner, A., and Igel, H. (2009). Inferring earth structure from combined measurements of rotational and translational ground motions. *Geophysics*, 74(6):WCD41–WCD47.
- Bernauer, M., Fichtner, A., and Igel, H. (2012). Measurements of translation, rotation and strain: new approaches to seismic processing and inversion. *Journal of Seismology*, 16(4):669–681.
- Bernauer, M., Fichtner, A., and Igel, H. (2014). Reducing nonuniqueness in finite source inversion using rotational ground motions. *Journal of Geophysical Research: Solid Earth*, 119(6):4860–4875.
- Bozdağ, E., Peter, D., Lefebvre, M., Komatsitsch, D., Tromp, J., Hill, J., Podhorszki, N., and Pugmire, D. (2016). Global adjoint tomography: first-generation model. *Geophysical Journal International*, 207(3):1739–1766.
- Brown, S. P., Thorne, M. S., Miyagi, L., and Rost, S. (2015). A compositional origin to ultralow-velocity zones. *Geophysical Research Letters*, 42(4):1039–1045.
- Burke, K., Steinberger, B., Torsvik, T. H., and Smethurst, M. A. (2008). Plume generation zones at the margins of large low shear velocity provinces on the core–mantle boundary. *Earth and Planetary Science Letters*, 265(1):49–60.
- Catalli, K., Shim, S.-H., and Prakapenka, V. (2009). Thickness and clapeyron slope of the post-perovskite boundary. *Nature*, 462(7274):782–785.
- Christensen, U. R. and Hofmann, A. W. (1994). Segregation of subducted oceanic crust in the convecting mantle. *Journal of Geophysical Research: Solid Earth*, 99(B10):19867–19884.
- Connolly, J. A. (2005). Computation of phase equilibria by linear programming: a tool for geodynamic modeling and its application to subduction zone decarbonation. *Earth and Planetary Science Letters*, 236(1-2):524–541.
- Cottaar, S., Martin, C., Li, Z., and Parai, R. (2022). The root to the galápagos mantle plume on the core–mantle boundary. *Seismica*, 1(1).
- Crotwell, H. P., Owens, T. J., and Ritsema, J. (1999). The TauP Toolkit: Flexible seismic travel-time and ray-path utilities. *Seismological Research Letters*, 70(2):154–160.
- Davaille, A., Le Bars, M., and Carbone, C. (2003). Thermal convection in a heterogeneous mantle. *Comptes Rendus Geoscience*, 335(1):141–156.
- Davies, G. and Dziewonski, A. (1975). Homogeneity and constitution of the Earth's lower mantle and outer core. *Physics of the Earth and Planetary Interiors*, 10(4):336–343.
- Deschamps, F., Cobden, L., and Tackley, P. J. (2012). The primitive nature of large low shear-wave velocity provinces. *Earth and Planetary Science Letters*, 349:198–208.
- Dorfman, S. M. and Duffy, T. S. (2014). Effect of Fe-enrichment on seismic properties of perovskite and post-perovskite in the deep lower mantle. *Geophysical Journal International*, 197(2):910–919.
- Durand, S., Debayle, E., Ricard, Y., Zaroli, C., and Lambotte, S. (2017). Confirmation of a change in the global shear velocity pattern at around 1000km depth. *Geophysical Journal International*, 211(3):1628–1639.
- Dziewonski, A. M. (1984). Mapping the lower mantle: determination of lateral heterogeneity in P velocity up to degree and order 6. *Journal of Geophysical Research: Solid Earth*, 89(B7):5929–5952.
- Dziewonski, A. M. and Anderson, D. L. (1981). Preliminary reference Earth model. *Physics of the Earth and Planetary Interiors*, 25(4):297 – 356.
- Dziewonski, A. M., Hager, B. H., and O'Connell, R. J. (1977). Large-scale heterogeneities in the lower mantle. *Journal of Geophysical Research*, 82(2):239–255.

- Fei, Y., Wang, Y., and Finger, L. W. (1996). Maximum solubility of FeO in (Mg, Fe) SiO₃-perovskite as a function of temperature at 26 GPa: Implication for FeO content in the lower mantle. *Journal of Geophysical Research: Solid Earth*, 101(B5):11525–11530.
- Fichtner, A. and Igel, H. (2009). Sensitivity densities for rotational ground-motion measurements. *Bulletin of the Seismological Society of America*, 99(2B):1302–1314.
- Ford, S. R., Garnero, E. J., and McNamara, A. K. (2006). A strong lateral shear velocity gradient and anisotropy heterogeneity in the lowermost mantle beneath the southern Pacific. *Journal of Geophysical Research: Solid Earth*, 111(B3).
- French, S. and Romanowicz, B. (2014). Whole-mantle radially anisotropic shear velocity structure from spectral-element waveform tomography. *Geophysical Journal International*, 199(3):1303–1327.
- Frost, D. A. and Rost, S. (2014). The P-wave boundary of the large-low shear velocity province beneath the Pacific. *Earth and Planetary Science Letters*, 403:380–392.
- Frost, D. J., Liebske, C., Langenhorst, F., McCammon, C. A., Trønnes, R. G., and Rubie, D. C. (2004). Experimental evidence for the existence of iron-rich metal in the Earth's lower mantle. *Nature*, 428(6981):409–412.
- Fullea, J., Lebedev, S., Martinec, Z., and Celli, N. L. (2021). WINTERC-G: mapping the upper mantle thermochemical heterogeneity from coupled geophysical–petrological inversion of seismic waveforms, heat flow, surface elevation and gravity satellite data. *Geophysical Journal International*, 226(1):146–191.
- Garnero, E. J. and Helmberger, D. V. (1995). A very slow basal layer underlying large-scale low-velocity anomalies in the lower mantle beneath the Pacific: evidence from core phases. *Physics of the Earth and Planetary Interiors*, 91(1-3):161–176.
- Garnero, E. J. and McNamara, A. K. (2008). Structure and dynamics of Earth's lower mantle. *Science*, 320(5876):626–628.
- Garnero, E. J., Revenaugh, J., Williams, Q., Lay, T., and Kellogg, L. H. (1998). Ultralow velocity zone at the core–mantle boundary. In *The Core–Mantle Boundary Region*, volume 28, pages 319–334. Wiley Online Library.
- Hansen, U. and Yuen, D. (2000). Extended-boussinesq thermal–chemical convection with moving heat sources and variable viscosity. *Earth and Planetary Science Letters*, 176(3):401–411.
- Harley, S. L. (1984). An experimental study of the partitioning of Fe and Mg between garnet and orthopyroxene. *Contributions to Mineralogy and Petrology*, 86(4):359–373.
- Harpp, K. S. and Weis, D. (2020). Insights into the origins and compositions of mantle plumes: A comparison of Galápagos and Hawai'i. *Geochemistry, Geophysics, Geosystems*, 21(9):e2019GC008887.
- He, Y. and Wen, L. (2009). Structural features and shear-velocity structure of the “Pacific Anomaly”. *Journal of Geophysical Research: Solid Earth*, 114(B2).
- He, Y., Wen, L., and Zheng, T. (2006). Geographic boundary and shear wave velocity structure of the “Pacific anomaly” near the core–mantle boundary beneath western Pacific. *Earth and Planetary Science Letters*, 244(1):302–314.
- Helffrich, G. R. and Wood, B. J. (2001). The Earth's mantle. *Nature*, 412(6846):501–507.
- Hernlund, J., Thomas, C., and Tackley, P. (2005). A doubling of the post-perovskite phase boundary and structure of the earth's lowermost mantle. *Nature*, 434(7035):882–886.
- Hirose, K., Brodholt, J., Lay, T., and Yuen, D. (2013). *Post-Perovskite: The Last Mantle Phase Transition*, volume 174. John Wiley & Sons.
- Hirose, K., Fei, Y., Ma, Y., and Mao, H.-K. (1999). The fate of subducted basaltic crust in the Earth's lower mantle. *Nature*, 397(6714):53–56.
- Hosseini, K., Matthews, K. J., Sigloch, K., Shephard, G. E., Domeier, M., and Tsekhnistrenko, M. (2018). SubMachine: Web-based tools for exploring seismic tomography and other models of Earth's deep interior. *Geochemistry, Geophysics, Geosystems*, 19(5):1464–1483.
- Igel, H., Schreiber, K. U., Gebauer, A., Bernauer, F., Egdorf, S., Simonelli, A., Liny, C.-J., Wassermann, J., Donner, S., Hadzioannou, C., et al. (2021). Romy: A multi-component ring laser for geodesy and geophysics. *Geophysical Journal International*, 225(1):684–698.
- Itaka, T., Hirose, K., Kawamura, K., and Murakami, M. (2004). The elasticity of the MgSiO₃ post-perovskite phase in the Earth's lowermost mantle. *Nature*, 430(6998):442–445.
- Ishii, M. and Tromp, J. (2004). Constraining large-scale mantle heterogeneity using mantle and inner-core sensitive normal modes. *Physics of the Earth and Planetary Interiors*, 146(1):113–124.
- Jensen, K. J., Thorne, M. S., and Rost, S. (2013). SPdKS analysis of ultralow-velocity zones beneath the western Pacific. *Geophysical Research Letters*, 40(17):4574–4578.
- Jordan, T. H. and Lynn, W. S. (1974). A velocity anomaly in the lower mantle. *Journal of Geophysical Research*, 79(17):2679–2685.
- Kaminsky, F. (2012). Mineralogy of the lower mantle: A review of ‘super-deep’ mineral inclusions in diamond. *Earth-Science Reviews*, 110(1-4):127–147.

- Kennett, B. and Engdahl, E. (1991). Traveltimes for global earthquake location and phase identification. *Geophysical Journal International*, 105(2):429–465.
- Kennett, B. L., Engdahl, E., and Buland, R. (1995). Constraints on seismic velocities in the Earth from traveltimes. *Geophysical Journal International*, 122(1):108–124.
- Kesson, S., Fitz Gerald, J., and Shelley, J. (1998). Mineralogy and dynamics of a pyrolite lower mantle. *Nature*, 393(6682):252–255.
- Khan, A., Boschi, L., and Connolly, J. (2009). On mantle chemical and thermal heterogeneities and anisotropy as mapped by inversion of global surface wave data. *Journal of Geophysical Research: Solid Earth*, 114(B9).
- King, S. D. and Anderson, D. L. (1998). Edge-driven convection. *Earth and Planetary Science Letters*, 160(3):289–296.
- Koolemeijer, P., Ritsema, J., Deuss, A., and Van Heijst, H.-J. (2016). SP12RTS: a degree-12 model of shear-and compressional-wave velocity for Earth's mantle. *Geophysical Journal International*, 204(2):1024–1039.
- Krischer, L., Megies, T., Barsch, R., Beyreuther, M., Lecocq, T., Caudron, C., and Wassermann, J. (2015). ObsPy: a bridge for seismology into the scientific Python ecosystem. *Computational Science and Discovery*, 8(1):014003.
- Lai, H., Garnero, E. J., Grand, S. P., Porritt, R. W., and Becker, T. W. (2019). Global travel time data set from adaptive empirical wavelet construction. *Geochemistry, Geophysics, Geosystems*, 20(5):2175–2198.
- Lay, T., Hernlund, J., and Buffett, B. A. (2008). Core–mantle boundary heat flow. *Nature geoscience*, 1(1):25–32.
- Lay, T., Hernlund, J., Garnero, E. J., and Thorne, M. S. (2006). A post-perovskite lens and D" heat flux beneath the central Pacific. *Science*, 314(5803):1272–1276.
- Lu, C. and Grand, S. P. (2016). The effect of subducting slabs in global shear wave tomography. *Geophysical Journal International*, 205(2):1074–1085.
- Lu, C., Grand, S. P., Lai, H., and Garnero, E. J. (2019). TX2019slab: A new P and S tomography model incorporating subducting slabs. *Journal of Geophysical Research: Solid Earth*, 124(11):11549–11567.
- Mao, W. L., Mao, H.-k., Sturhahn, W., Zhao, J., Prakapenka, V. B., Meng, Y., Shu, J., Fei, Y., and Hemley, R. J. (2006). Iron-rich post-perovskite and the origin of ultralow-velocity zones. *Science*, 312(5773):564–565.
- Maruyama, S., Santosh, M., and Zhao, D. (2007a). Superplume, supercontinent, and post-perovskite: mantle dynamics and anti-plate tectonics on the core–mantle boundary. *Gondwana Research*, 11(1-2):7–37.
- Maruyama, S., Santosh, M., and Zhao, D. (2007b). Superplume, supercontinent, and post-perovskite: mantle dynamics and anti-plate tectonics on the core–mantle boundary. *Gondwana Research*, 11(1):7 – 37.
- McDonough, W. F. and Sun, S.-S. (1995). The composition of the Earth. *Chemical Geology*, 120(3-4):223–253.
- McNamara, A. K. (2019). A review of large low shear velocity provinces and ultra low velocity zones. *Tectonophysics*, 760:199–220.
- McNamara, A. K., Garnero, E. J., and Rost, S. (2010). Tracking deep mantle reservoirs with ultra-low velocity zones. *Earth and Planetary Science Letters*, 299(1):1–9.
- McNamara, A. K. and Zhong, S. (2004). Thermochemical structures within a spherical mantle: Superplumes or piles? *Journal of Geophysical Research: Solid Earth*, 109(B7).
- McNamara, A. K. and Zhong, S. (2005). Thermochemical structures beneath Africa and the Pacific Ocean. *Nature*, 437(7062):1136–1139.
- Métaxian, J.-P., Lesage, P., and Valette, B. (2002). Locating sources of volcanic tremor and emergent events by seismic triangulation: Application to Arenal volcano, Costa Rica. *Journal of Geophysical Research: Solid Earth*, 107(B10):ECV–10.
- Morelli, A. and Dziewonski, A. M. (1993). Body wave traveltimes and a spherically symmetric P-and S-wave velocity model. *Geophysical Journal International*, 112(2):178–194.
- Moulik, P. and Ekström, G. (2014). An anisotropic shear velocity model of the earth's mantle using normal modes, body waves, surface waves and long-period waveforms. *Geophysical Journal International*, 199(3):1713–1738.
- Mula, A. H. and Müller, G. (1980). Ray parameters of diffracted long period P and S waves and the velocities at the base of the mantle. *pure and applied geophysics*, 118:1272–1292.
- Müntener, O. and Ulmer, P. (2018). Arc crust formation and differentiation constrained by experimental petrology. *American Journal of Science*, 318(1):64–89.
- Murakami, M., Hirose, K., Kawamura, K., Sata, N., and Ohishi, Y. (2004). Post-perovskite phase transition in MgSiO₃. *Science*, 304(5672):855–858.
- Murakami, M., Ohishi, Y., Hirao, N., and Hirose, K. (2012). A perovskitic lower mantle inferred from high-pressure, high-temperature sound velocity data. *Nature*, 485(7396):90–94.

- Nakagawa, T., Tackley, P. J., Deschamps, F., and Connolly, J. A. (2009). Incorporating self-consistently calculated mineral physics into thermochemical mantle convection simulations in a 3-D spherical shell and its influence on seismic anomalies in Earth's mantle. *Geochemistry, Geophysics, Geosystems*, 10(3).
- Nakagawa, T., Tackley, P. J., Deschamps, F., and Connolly, J. A. (2010). The influence of MORB and harzburgite composition on thermo-chemical mantle convection in a 3-D spherical shell with self-consistently calculated mineral physics. *Earth and Planetary Science Letters*, 296(3-4):403–412.
- Ni, S., Tan, E., Gurnis, M., and Helmberger, D. (2002). Sharp sides to the African superplume. *Science*, 296(5574):1850–1852.
- Nolet, G., Hello, Y., Lee, S. v. d., Bonniewx, S., Ruiz, M. C., Pazmino, N. A., Deschamps, A., Regnier, M. M., Font, Y., Chen, Y. J., et al. (2019). Imaging the galápagos mantle plume with an unconventional application of floating seismometers. *Scientific reports*, 9(1):1326.
- Oganov, A. R. and Ono, S. (2004). Theoretical and experimental evidence for a post-perovskite phase of mgsio_3 in earth's d'' layer. *Nature*, 430(6998):445–448.
- Palme, H. and O'Neill, H. (2007). 2.01 - Cosmochemical Estimates of Mantle Composition. In Holland, H. D. and Turekian, K. K., editors, *Treatise on Geochemistry*, pages 1–38. Pergamon, Oxford.
- Parsons, B. and McKenzie, D. (1978). Mantle convection and the thermal structure of the plates. *Journal of Geophysical Research: Solid Earth*, 83(B9):4485–4496.
- Reinwald, M., Bernauer, M., Igel, H., and Donner, S. (2016). Improved finite-source inversion through joint measurements of rotational and translational ground motions: a numerical study. *Solid Earth*, 7(5):1467–1477.
- Ritsema, J., Deuss, A., van Heijst, H. J., and Woodhouse, J. H. (2011). S40RTS: a degree-40 shear-velocity model for the mantle from new Rayleigh wave dispersion, teleseismic traveltimes and normal-mode splitting function measurements. *Geophysical Journal International*, 184(3):1223–1236.
- Ritsema, J., van Heijst, H. J., and Woodhouse, J. H. (1999). Complex shear wave velocity structure imaged beneath Africa and Iceland. *Science*, 286(5446):1925–1928.
- Rost, S. and Garnero, E. J. (2006). Detection of an ultralow velocity zone at the core-mantle boundary using diffracted PKPab waves. *Journal of Geophysical Research: Solid Earth*, 111(B7):B07309.
- Rost, S., Garnero, E. J., and Stefan, W. (2010). Thin and intermittent ultralow-velocity zones. *Journal of Geophysical Research: Solid Earth*, 115(B6).
- Rost, S., Garnero, E. J., and Williams, Q. (2006). Fine-scale ultralow-velocity zone structure from high-frequency seismic array data. *Journal of Geophysical Research: Solid Earth*, 111(B9).
- Rost, S. and Revenaugh, J. (2003). Small-scale ultralow-velocity zone structure imaged by ScP. *Journal of Geophysical Research: Solid Earth*, 108(B1).
- Rost, S. and Thomas, C. (2002). Array seismology: Methods and applications. *Reviews of Geophysics*, 40(3):2–1.
- Schubert, G., Masters, G., Olson, P., and Tackley, P. (2004). Superplumes or plume clusters? *Physics of the Earth and Planetary Interiors*, 146(1-2):147–162.
- Shim, S.-H. (2008). The postperovskite transition. *Annu. Rev. Earth Planet. Sci.*, 36(1):569–599.
- Shim, S.-H., Kubo, A., and Duffy, T. S. (2007). Raman spectroscopy of perovskite and post-perovskite phases of MgGeO_3 to 123 GPa. *Earth and Planetary Science Letters*, 260(1):166–178.
- Sinmyo, R., Ozawa, H., Hirose, K., Yasuhara, A., Endo, N., Sata, N., and Ohishi, Y. (2008). Ferric iron content in $(\text{Mg}, \text{Fe})\text{SiO}_3$ perovskite and post-perovskite at deep lower mantle conditions. *American Mineralogist*, 93(11-12):1899–1902.
- Souriau, A. and Poupinet, G. (1994). Lateral variations in P velocity and attenuation in the D'' layer, from diffracted P waves. *Physics of the earth and planetary interiors*, 84(1-4):227–234.
- Stackhouse, S., Brodholt, J. P., Dobson, D. P., and Price, G. D. (2006). Electronic spin transitions and the seismic properties of ferrous iron-bearing MgSiO_3 post-perovskite. *Geophysical research letters*, 33(12).
- Stein, S. and Wyssession, M. (2009). *An Introduction to Seismology, Earthquakes, and Earth Structure*. John Wiley & Sons.
- Sun, D. and Miller, M. S. (2013). Study of the western edge of the African large low shear velocity province. *Geochemistry, Geophysics, Geosystems*, 14(8):3109–3125.
- Sun, N., Wei, W., Han, S., Song, J., Li, X., Duan, Y., Prakapenka, V. B., and Mao, Z. (2018). Phase transition and thermal equations of state of (Fe, Al)-bridgmanite and post-perovskite: Implication for the chemical heterogeneity at the lowermost mantle. *Earth and Planetary Science Letters*, 490:161–169.
- Suzuki, Y., Kawai, K., Geller, R. J., Tanaka, S., Siripunvaraporn, W., Boonchaisuk, S., Noisagool, S., Ishihara, Y., and Kim, T. (2020). High-resolution 3-D S-velocity structure in the D'' region at the western margin of the Pacific LLSVP: Evidence for small-scale plumes and paleoslabs. *Physics of the Earth and Planetary Interiors*, 307:106544.

- Tackley, P. J. (1998). *Three-Dimensional Simulations of Mantle Convection with a Thermo-Chemical Basal Boundary Layer: D''?*, pages 231–253. American Geophysical Union (AGU).
- Tanaka, S., Suetsugu, D., Shiobara, H., Sugioka, H., Kanazawa, T., Fukao, Y., Barrool, G., and Reymond, D. (2009). On the vertical extent of the large low shear velocity province beneath the south Pacific superswell. *Geophysical Research Letters*, 36(7):L07305.
- Tateno, S., Hirose, K., Sata, N., and Ohishi, Y. (2007). Solubility of FeO in (Mg, Fe) SiO₃ perovskite and the post-perovskite phase transition. *Physics of the Earth and Planetary Interiors*, 160(3-4):319–325.
- Tateno, S., Hirose, K., Sata, N., and Ohishi, Y. (2009). Determination of post-perovskite phase transition boundary up to 4400 K and implications for thermal structure in D'' layer. *Earth and Planetary Science Letters*, 277(1-2):130–136.
- Tesoniero, A., Auer, L., Boschi, L., and Cammarano, F. (2015). Hydration of marginal basins and compositional variations within the continental lithospheric mantle inferred from a new global model of shear and compressional velocity. *Journal of Geophysical Research: Solid Earth*, 120(11):7789–7813.
- Thorne, M. S., Garnero, E. J., Jahnke, G., Igel, H., and McNamara, A. K. (2013a). Mega ultra low velocity zone and mantle flow. *Earth and Planetary Science Letters*, 364:59–67.
- Thorne, M. S., Zhang, Y., and Ritsema, J. (2013b). Evaluation of 1-D and 3-D seismic models of the Pacific lower mantle with S, SKS, and SKKS traveltimes and amplitudes. *Journal of Geophysical Research: Solid Earth*, 118(3):985–995.
- Trifunac, M. D. (2006). Effects of torsional and rocking excitations on the response of structures. In *Earthquake Source Asymmetry, Structural Media and Rotation Effects*, pages 569–582. Springer.
- Tsuchiya, T. and Tsuchiya, J. (2006). Effect of impurity on the elasticity of perovskite and postperovskite: Velocity contrast across the postperovskite transition in (Mg, Fe, Al)(Si, Al) O₃. *Geophysical Research Letters*, 33(12).
- Tsuchiya, T., Tsuchiya, J., Umemoto, K., and Wentzcovitch, R. M. (2004). Phase transition in MgSiO₃ perovskite in the Earth's lower mantle. *Earth and Planetary Science Letters*, 224(3-4):241–248.
- Turcotte, D. L. and Schubert, G. (2002). *Geodynamics*. Cambridge university press.
- Vanacore, E. and Niu, F. (2011). Characterization of the D'' beneath the Galapagos Islands using SKKS and SKS waveforms. *Earthquake Science*, 24:87–99.
- Vanacore, E., Rost, S., and Thorne, M. (2016). Ultralow-velocity zone geometries resolved by multidimensional waveform modelling. *Geophysical Journal International*, 206(1):659–674.
- Vilella, K., Bodin, T., Boukaré, C.-E., Deschamps, F., Badro, J., Ballmer, M. D., and Li, Y. (2021). Constraints on the composition and temperature of LLSPVs from seismic properties of lower mantle minerals. *Earth and Planetary Science Letters*, 554:116685.
- Villagómez, D. R., Toomey, D. R., Geist, D. J., Hooft, E. E., and Solomon, S. C. (2014). Mantle flow and multistage melting beneath the galápagos hotspot revealed by seismic imaging. *Nature Geoscience*, 7(2):151–156.
- Wang, J., Lekić, V., Schmerr, N. C., Gu, Y. J., Guo, Y., and Lin, R. (2024). Mesozoic intraoceanic subduction shaped the lower mantle beneath the East Pacific Rise. *Science Advances*, 10(39):eado1219.
- Wang, Y. and Wen, L. (2004). Mapping the geometry and geographic distribution of a very low velocity province at the base of the Earth's mantle. *Journal of Geophysical Research: Solid Earth*, 109(B10).
- Wen, L. and Helmberger, D. V. (1998). Ultra-low velocity zones near the core-mantle boundary from broadband PKP precursors. *Science*, 279(5357):1701–1703.
- Wentzcovitch, R. M., Tsuchiya, T., and Tsuchiya, J. (2006). MgSiO₃postperovskite at D'' conditions. *Proceedings of the national academy of sciences*, 103(3):543–546.
- Williams, Q., Jeanloz, R., and McMillan, P. (1987). Vibrational spectrum of MgSiO₃ perovskite: Zero-pressure Raman and mid-infrared spectra to 27 GPa. *Journal of Geophysical Research: Solid Earth*, 92(B8).
- Wookey, J., Stackhouse, S., Kendall, J.-M., Brodholt, J., and Price, G. D. (2005). Efficacy of the post-perovskite phase as an explanation for lowermost-mantle seismic properties. *Nature*, 438(7070):1004–1007.
- Workman, R. K. and Hart, S. R. (2005). Major and trace element composition of the depleted MORB mantle (DMM). *Earth and Planetary Science Letters*, 231(1-2):53–72.
- Zhang, Y., Ritsema, J., and Thorne, M. S. (2009). Modeling the ratios of SKKS and SKS amplitudes with ultra-low velocity zones at the core-mantle boundary. *Geophysical Research Letters*, 36(19):L19303.